WAVELET ANALYSIS APPLIED TO THE IRAS CIRRUS

WILLIAM D. LANGER
MS 169-506, Jet Propulsion Laboratory, Caltech, Pasadena, CA 91109

ROBERT W. WILSON
HOH-L239, AT&T Bell Laboratories, Holmdel, NJ 07733

CHARLES H. ANDERSON
Box 8108, Washington University School of Medicine, St. Louis, MO 63110

ABSTRACT The structure of infrared cirrus clouds is analyzed with Laplacian pyramid transforms, a form of non-orthogonal wavelets. Pyramid and wavelet transforms provide a means to decompose images into their spatial frequency components such that all spatial scales are treated in an equivalent manner. The multiscale transform analysis is applied to IRAS 100 μm maps of cirrus emission in the north Galactic pole region to extract features on different scales. In the maps we identify filaments, fragments and clumps by separating all connected regions. These structures are analyzed with respect to their Hausdorff dimension for evidence of the scaling relationships in the cirrus clouds.

INTRODUCTION

In general, interstellar clouds appear inhomogeneous with features on different scale size depending on the spatial resolution of the telescope and the tracer used to probe the structure. This structure results from a fragmentation process that is not well understood and cannot be easily modeled because of the non-linear nature of the hydrodynamic equations which describe the cloud evolution. The formation and evolution of interstellar clouds is governed by a variety of forces including gravity, magnetic fields, rotation, thermal pressure, turbulence, and systematic motions. In addition discrete stellar sources inject energy into the clouds in the form of winds and shocks, producing systematic and turbulent motion. A highly "clumpy" or fragmented structure may reflect gravitational fragmentation or the presence of turbulence resulting from the cascade and redistribution of energy injected on different scales. In contrast, a highly filamentary structure might result from ordered magnetic fields.

To study the structure and dynamics of interstellar clouds observers have mapped them on different scales and to different degrees, mainly with the isotopes of CO, CS, and the 100 and 60 μm infrared dust emission, each of which traces a different aspect of the density and mass distribution. Interpreting these

S. Terebey and J. Mazzarella (eds.), *Science with High-Spatial Resolution Far Infrared Data*, 143–155, 1994, Jet Propulsion Laboratory, Pasadena, CA.

maps has proven to be more complicated because one does not know *a priori* what kind of features to extract and exactly how the distribution of features, their sizes and number, relate to the dynamics of the cloud.

To interpret the maps one needs some method to extract structural features and determine their number, size, distribution, mass, and energy content. Several approaches have been applied and discussed in the literature including a search for connected objects (Dickman, Horvath, and Margulis 1990; Falgarone, Phillips, and Walker 1991), the autocorrelation function, the structure function (Kleiner and Dickman 1984 and 1985), an iterative fitting procedure assuming Gaussian-shaped clumps (Stutzki and Gusten 1990) and structure tree analysis (Houlahan and Scalo 1990 and 1992). Recently we suggested that Laplacian pyramid (multiscale) transforms (LPT) are more suitable for determining the structure of interstellar clouds (Langer, Wilson, and Anderson 1993).

The best known example of the multiscale transform is the wavelet transform (Grossman and Morlet 1987; see also the reviews by Daubechies 1992; Farge 1992). Multiscale transforms provide a mathematically consistent way to extract structural components and map properties from astronomical images. The multiscale transform has been characterized as a generalization of the Fourier Transform which is capable of representing a function in terms of spatial and frequency localization. The localized structures at different scales are easier to identify in the transformed space than in the original (x, y) space. The wavelet transform is well suited to provide detailed information and deep insight into structure. Orthonormal wavelets have been used to extract particular features from complex astronomical data, including: galaxy counts (Slezak, Bijaoui, and Mars 1990; Martinez, Paredes, and Saar 1993); stellar photometry in globular clusters (Auriere and Coupinot 1989); ^{13}CO spectral data of the L1551 outflow (Gill and Henricksen 1990); and, photometric analysis of galaxies (Coupinot et al. 1992).

Here we apply a multiscale transform analysis of infrared cirrus clouds in the North Polar region using the IRAS Sky Survey Atlas (Wheelock et. al. 1994) plates and analyze the fractal structure and morphology of the clouds. Infrared 60 and 100 μm IRAS maps have been analyzed for scale-dependent morphology by a number of authors using algorithms to characterize the features which rely on connecting contours in the original (x, y) intensity maps. Bazell and Désert (1988) analyzed the fractal structure of interstellar cirrus using the Skyflux plates for three regions: one above and one below the plane ($b = +23°$ and $-14°$) and a third region at $b = -40°$ containing two well known high-latitude MBM clouds. Dickman, Horvath, and Margulis (1990) analyzed IRAS images of five molecular cloud complexes (including the well known regions of Chameleon, ρ Oph, and Taurus). Both studies found a highly fractal structure for the clouds and concluded that the clouds had a highly turbulent structure. However, they differ in the behavior of the scaling from region to region, which might not be surprising considering that one concentrates on molecular and the other diffuse regions. Our multiscale analysis of cirrus emission reveals a more complex structure than either of these previous studies.

MULTISCALE TRANSFORMS

First, we review the various multiscale transforms (Pyramids and Wavelets) and compare them to Fourier Transforms. Laplacian pyramid transforms preceded and spurred the recent interest by mathematicians in the more formalized orthogonal wavelets. In practice the orthogonal wavelets have proven useful primarily in image data compression, while the Laplacian pyramid has remained more useful for carrying out a variety of image analysis tasks.

Fourier Transform

A Fourier Transform decomposes a function $f(x)$ into a linear composition of Fourier vectors, whose basis functions are sines and cosines, defined by their Fourier coefficients,

$$\hat{f}(k) = (2\pi)^{-1/2} \int f(x) e^{ikx} dx. \tag{1}$$

Unfortunately e^{ikx} oscillates forever and the information content of $f(x)$ is delocalized among all the spectral coefficients $\hat{f}(k)$. Regions of $f(x)$ that vary sharply – for example a delta function – have their information spread among all of k space. Such transform properties are not very useful for real astronomical images which contain a great deal of structure.

One approach to achieve localization is to use a window to isolate the portion of the frequency or spatial scale of interest. Windowed transforms can also be applied sequentially to recover all of the function, however such transforms use fixed window size and thus do not analyze the function at all scales. An example of a windowed transform is the Gabor transform,

$$G^a(x) = (4\pi a)^{-1/2} \, e^{-x^2/4a} \tag{2}$$

which uses a Gaussian window. The real part of the transform of the Gabor function, ReG_ω is shown in Figure 1 for three values of ω; note that the Gabor transform has a fixed window size and that the transformed G oscillate within a fixed envelope.

Wavelet Transform

The wavelet transform localizes information in space and scale and the decomposition is done by translation and dilation of a single "Parent" function, the analyzing wavelet. The wavelet transform is defined by

$$T_g(a,b) = |a|^{-1/2} \int_{-\infty}^{\infty} f(x) g\{(x-b)/a\} dx \tag{3}$$

where the factor a covers different ranges in scale (frequency) and b moves the localization center (position or time). The wavelet transform separates data or functions into different spatial components and analyzes each component with a resolution to match its scale. The wavelet transform function must have the property that its mean is zero over x,

$$\int_{-\infty}^{\infty} g(x) dx = 0. \tag{4}$$

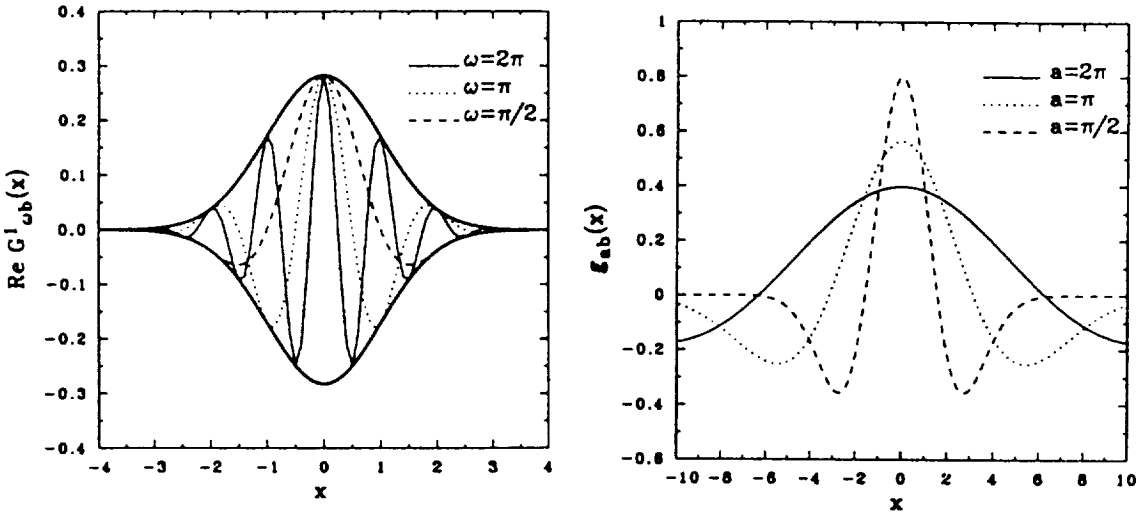

FIGURE 1 The functions g_{ab} and $ReG_{\omega b}$ for three values of a and ω (b = 0). The Gabor transform has a fixed window size in contrast to the wavelet transform's flexible window (Martinez et al. 1993).

One of the best known examples of a wavelet transform in astronomy is the Marr (or "Mexican Hat") wavelet, which in one dimension has the form,

$$g(z) = (1 - z^2)\epsilon^{-z2/2}, \quad \text{where } z = (x - b)/a \tag{5}$$

The transformed function g_{ab} is shown in Figure 1 for three values of a (assuming b = 0) where one can see that the Marr wavelet has a flexible window size. Wavelets have the useful property that they preserve scaling behavior and are sensitive to signal variations but not to constant behavior. They also provide a useful description of turbulence because they retain information about the spatial structure of the flow (c.f. the review by Farge 1992).

Discrete Wavelet Transform

There is a discrete wavelet transform (DWT) analogous to the discrete Fourier transform (DFT), both of which are rotations in function space, but take an input space into different domains. For the DFT the basis functions are unit vectors or Dirac delta functions (in the continuum limit). For the DFT the domain has sine and cosine basis functions, while for the DWT they are localized in space. The best known examples of the DWT use the Daubechies basis functions (Daubechies 1992). We do not have space to review the DWT (see Press et al. 1993) but point out that the transform is a matrix whose odd and even rows perform different convolutions: the odd rows generate components of the data convolved with filter coefficients and perform a moving average with the smoothing filter H; the even rows perform a convolution with a filter L which represents the detailed information in the data. The DWT is applied hierarchically to the data vector (i.e., first to the full length data N, then to the "smooth" vector of length N/2, etc.) ultimately producing a set of wavelet coefficients that represent the smoothed information on the largest scale and

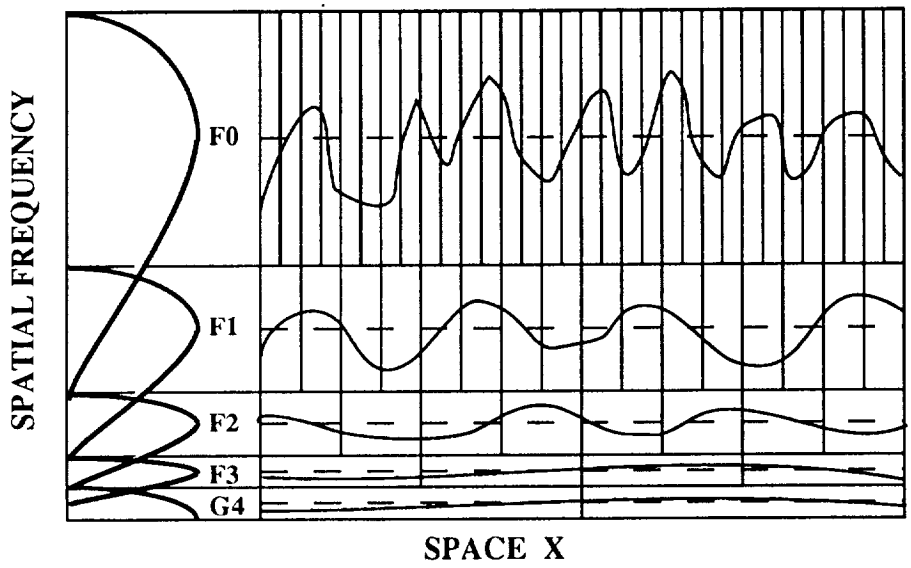

FIGURE 2 Scale invariant filter bank: Filter responses, $F_n(k) = F_0(2^n k)$, on the left.

detailed information on scales differing by factors of two. Specific examples are given by Daubechies (1992) and Press et al. (1993).

Pyramid Transforms

Pyramid transforms preceded and spurred the recent interest by mathematicians in the more formalized orthogonal wavelets. However, one of the major difficulties with the orthogonal wavelets is that, while their basis functions display shift and scale invariant properties, the coefficients in these expansions do not (see Strang 1989; Simoncelli et al. 1992). The fact that the power within a given scale is not invariant to translations of the input should be enough to make one wary. In addition, when implemented as separable filters, the orthogonal wavelet transform creates three highly anisotropic bandpass components at each scale, which have no simple relationship to underlying physical properties.

Pyramid transforms provide a means to decompose images into their spatial frequency components such that all spatial scales are treated in an equivalent manner. The concepts are equally applicable to data of any dimension, where each axis represents some continuous physical parameter such as spectral wavelength, time, or in the case of images vertical and horizontal lengths or angular displacements. An intuitive grasp of the idea can be obtained in one dimension by considering the illustration in Figure 2. The horizontal axis represents a parameter such as space and the vertical axis spatial frequency. If we consider a signal $S(x)$ that has been bandpass limited by a fixed amount, then it can represented by a uniform sequence of samples $S(x_i)$, as set by the Nyquist sampling theorem, with no loss of information. Now consider passing the signal through a bank of filters that are scaled copies of one another, such that $F_n(k) = F_0(2^n k)$,

where the scaling by factors of two is chosen for convenience. The output of each filter treats the signal in a scale invariant fashion because of the scaling relationship between the filters. The outputs of each filter must be sampled at a rate that is proportional to the corresponding bandwidth, hence each band is sampled at a rate that differs from its neighbors by a factor of two, as illustrated in Figure 2. This method of signal decomposition is the basis of all scale invariant multiresolution representations such as Pyramids and Wavelets. The signal processing community have labeled them as a special class of subband encoding schemes.

The generality of this form of signal analysis is best illustrated by noting that the human visual and auditory systems utilize it. The scale invariant nature of many physical processes is what makes these representations important. The statistics of the signals and the forms of the structures produced by these filters provide measures of how underlying physical processes change with scale. The coefficients in these representations are much more statistically independent of one another than they are in the original data formats, which leads to a rich set of localized descriptors of images and better data compression for storage.

The number of such decompositions is large since there are many filter designs whose scaled filter banks will cover the frequency range of interest with sufficient density to prevent loss of information. This means there is a multitude of possible multiscale transforms unlike the Fourier transform. The choice of which filter to use is determined by factors such as efficiency of computation, signal-to-noise ratios, information storage and the type of data analysis one desires to perform. When one goes into higher dimensional spaces the choices for the shape of the filter become increasingly more flexible and hence increase the number of possible transforms. The orthonormal wavelets, which have recently received a lot of recognition, are a particular subset of the multiscale transforms. These provide critically sampled representations with minimal storage, as well as having some nice mathematical properties, but the constraint of orthogonality leads to filter designs that are not necessarily the best for many applications. There are a number of overcomplete transforms, such as the Laplacian pyramid, based on circularly symmetric filters, oriented pyramids, which have "wavelet"-like filters, and a recent new class with a property called "shiftability" (cf. Strang 1989, Simoncelli et al. 1992).

The Laplacian pyramids are best understood as the outputs of a bank of scaled circularly symmetric, bandpass spatial frequency filters, with center frequencies $k_n = k_0/2^n$ and roughly octave bandwidths. The simple variant used here is called an FSD (Filter, Subtract, and Decimate) pyramid (cf. Van der Wal 1991). Starting with the original image, designated as $G_0(x, y)$, the following rules are applied recursively to create a sequence of lowpass images (or Gaussian levels) $G_n(x, y)$ and bandpass (or Laplacian levels) $L_n(x, y)$:

$$\hat{G}_{n+1} = H * G_n \quad \{\textbf{Filter}\} \tag{6}$$

$$L_n = G_n - \hat{G}_{n+1} \quad \{\textbf{Subtract}\} \tag{7}$$

$$G_{n+1} = \{\textbf{Decimate}\} \quad \hat{G}_{n+1} \tag{8}$$

The filter operation $H * G_n$ involves convolving the image G_n with a lowpass filter H. A separable filter, $H(x,y) = h(x)h(y)$, was used in this work, where we adopted a five tap filter for $h(x)$ having the tap values 1/16, 1/4, 3/8, 1/4, 1/16, which produces an approximately circularly symmetric filter in the spatial frequency domain. The Laplacian components, L_n, are computed by subtracting the low pass version from the unblurred one at each scale. This operation is equivalent to filtering with a "Mexican hat" or difference of a Gaussian-like shaped kernal. The blurred version, G_n, is then subsampled by throwing away every other pixel and row, which is traditionally called "decimation." Decimation is justified because the lowpass filter reduces the spatial frequency content such that little aliasing is introduced by this process. Since this reduces the number of pixel values by four at each stage in a two-dimensional map, the computation of all the levels L_1 to L_N takes only one third the time and resources to compute L_0. Typically the final level N is set by stopping the process when the smallest dimension of the array $G_{n+1}(x,y)$ would be no smaller than eight. Mathematically, the set of values $L_n(x,y)$ for $n = 0$ to N plus G_{N+1}, constitute the components of an overcomplete non-orthogonal wavelet decomposition of the original image G_0. The bandpass components show less than two percent anisotropic response to spatial frequency orientation and less than five percent to translation of the input image. This operation is a computationally efficient, basic wavelet transform that has a relationship to some simple multiscale statistics. The G_n are mean values computed over regions that increase in size by factors of two and the L_n provide the local deviations from these multiscale mean values.

IRAS IMAGES OF THE NORTH POLAR CIRRUS

To analyze the structure of cirrus emission we have chosen a region in the north Galactic pole (declination 90° at map center) in order to minimize the line-of-sight confusion. We obtained 60 and 100 μm images of the North Polar Cirrus from the ISSA data measuring 5° on a side with pixels of $1.5' \times 1.5'$, although the actual resolution of the images is closer to $4'$ (the IRAS beam size at 100 μm). Figure 3 is a contour plot of the 100 μm image and shows the highly complex filamentary and globular nature of the emission. From the 100 and 60 μm images one can calculate a dust color temperature and opacity assuming a one component model of the dust grains (cf. Langer et al. 1989). The color temperature map is roughly uniform with a temperature of 25 K and the temperature drops in the regions of brightest emission where the opacity is a minimum. This behavior is well known for the 60 and 100 μm maps and is a result of using an overly simplified grain emission model. Therefore we decided to restrict our analysis to the 100 μm maps as the 100 μm emission arises from cooler dust, is optically thin, and thus more likely to arise uniformly from all the material along the line-of-sight. The 100 μm maps show a great deal of structure on all scales and the variation in emission is either due to increased column density, changing dust grain distribution, or variations in heating sources.

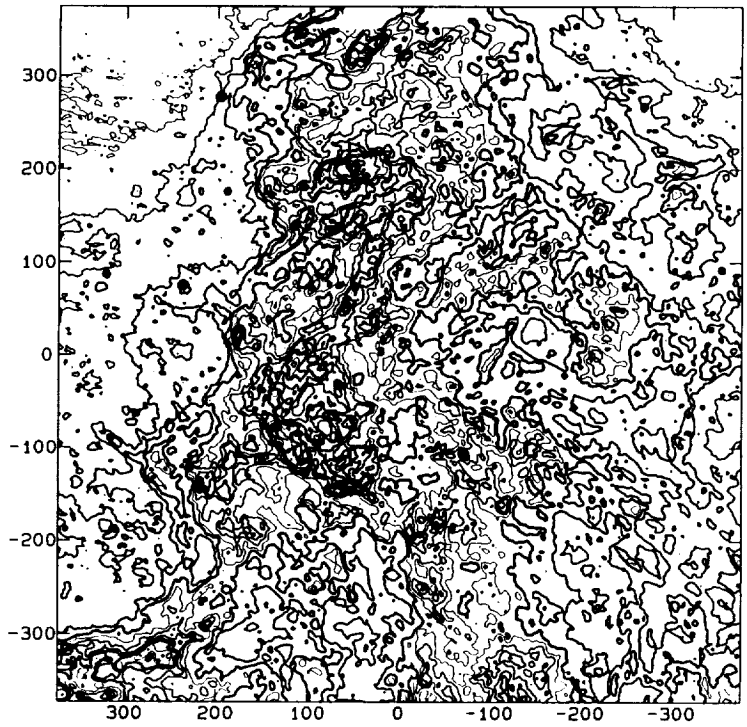

FIGURE 3 The 100 μm image of the North Polar Cirrus (dec = 90°, 0^h is at the top and RA goes counterclockwise with 6^h on the left); the axes are in arcmin with respect to the center. Intensity units range from 2 to 16 $\times$ 10^6.

RESULTS

The LPT applied to the 100 μm image of the North Polar Cirrus generates a set of amplitude maps for each of the basis functions, ranging from L_0 to L_5 covering the smallest to largest scales (1.5′ to 9′), and G_5 (the original image is labeled G_0). The G_n are mean values computed over regions that increase in size by factors of two and the L_n provide the local deviations from these multiscale values. The Ln images represent the detailed information and have equal positive and negative areas (average over the maps is zero). G_5, which has a resolution of 48′, is smooth and positive definite over the map. There is not room here to display the Laplacian images but examples of the transform maps for CO clouds can be seen in Langer et al. (1993).

To extract the structure in the map we assume that at each scale the features are embedded one within the other, or superimposed along the line-of-sight. We define a clump or filament as a connected region of positive amplitude, that is the zero contour boundary in the Laplacian maps. Bubbles or valleys would correspond to connected negative regions. (These maps are better for isolating features because of the separation of different scales and the preservation of locality in the transformed space.)

For each image we can determine the following properties of the connected positive or negative regions:

Perimeter = P,

Area = A,

Intensity = $\int \phi(x, y) dA$,

where $\phi(x, y)$ = amplitude of the wavelet basis function at (x, y),

Brightness = $[\int \phi(x, y) dA]/A$,

rms = $\int |\phi(x, y)|^2 dA$.

The major problem with this approach is that there are many features at small scale that correspond to noise in the maps or are on smaller scales than the beam resolution (the pixel area is 2.25 arcmin^2 while the IRAS beam is roughly 3′ to 4′). We avoid this problem by only considering features whose area, A, is greater than 16 arcmin^2). Table 1 summarizes the number of distinct features of positive amplitude for each of the Laplacian maps.

TABLE 1 Summary of Cirrus Features in Each LPT Basis Map

Order (1)	$(\Delta\lambda)^*$ (′)	Number of Features
0	1.5	1423
1	3.0	684
2	6.0	252
3	12.0	81
4	24.0	28
5	48.0	11

* The wavelength of each band is approximated by the width, $\Delta\lambda$, of each high pass filter.

Here we concentrate on only one property of the structure analysis of the cirrus clouds, the scale-dependent morphology, or fractal structure. One widely used approach to measuring the morphology of the cloud structures is the Hausdorff dimension (Bazell and Désert 1988, Dickman et al. 1990) which is the fractal dimension of the objects in the cloud. The fractals are self-similar under scale changes and so a determination of the Hausdorff dimension, D, can help identify the scale-dependent morphology of the cloud. Ideally, the geometrical structures and the scale dependence provide information about the forces at work in the cloud. D is defined as

$$A^{1/2} = K P^{1/D} \tag{9}$$

where a plot of log perimeter versus log area yields a slope of $D/2$ and has an intercept equal to $-D(\log K)$. Regular geometrical objects (circles, ellipses, squares, etc.) all have $D = 1$ (i.e., the same scaling) but different intercepts (i.e., K depends on shape). A value of $D \approx 4/3$ characterizes the relationship

expected for Kolmogorov turbulence (incompressible, homogeneous, isotropic turbulence); see the discussion by Dickman et al. Filamentary structures that scale only with length, on the other hand, have $D \approx 2$, as would be characteristic of gas supported by magnetic fields in the radial direction. Figure 4 shows an example of the plot of log(P) versus log(A) for the $l = 1$ image ($\Delta\lambda \approx 3'$). Note that the fit is not particularly good for large areas ($A > 400$ arcmin^2). For the small wavelengths ($l = 0$ and 1) the fits are dominated by the many small features in the map (note each cross in Figure 4 can represent many clumps of the same area and perimeter). Figure 5a plots D as a function of the l value and shows relatively little variation with wavelength. The log(P)-log(A) fits for $l = 4$ and 5 do not have much area dependence and the average value for D in Figure 5 is about 1.45. Bazell and Désert found a rather different average value, $D \approx 1.25$, for the cirrus clouds, however, there was variation within each image (see their Figure 2). Dickman et al.'s study of 100 μm maps of molecular regions found D ranging from 1.2 to 1.3, similar to those found for cirrus clouds (remember that these results use a completely different method than that discussed here to determine the map features).

Determining the Hausdorff dimension as a function of area, in the sense of considering several ranges of area within an l map, yields somewhat different results. Figure 5b plots D for the $l = 1$ image divided up into four different ranges. For the smallest features the Hausdorff dimension is 1.25, similar to the result of Bazell and Désert, but it increases with area reaching a value about 2 for the largest objects in the image. As the $l = 1$ map corresponds to features that respond to a multiscale filter of about $3'$ (in at least one direction) the largest features resemble thin filamentary or web-like structures. This result suggests that the forces that control the structure at large and small scales in the cirrus map of the north pole region are different.

DISCUSSION

D for all the North Polar Cirrus features ranges from 1.35 to 1.5 with an average of 1.45 for all the Laplacian maps. These values are larger than the average value of 1.25 found by Bazell and Désert in three cirrus maps, their maximum value of 1.40 for plate 2, and the values for $D(\approx 1.18 - 1.28)$ for 100 μm IRAS maps of the molecular clouds studied by Dickman et al. It is not clear if the differences are due to the choice of objects or the method to extract the map features. We will analyze the Chameleon region in the near future to test the latter possibility. The fractal nature of the cloud B5 studied with CO maps (Langer et al.) has D ranging from 1.3 to 1.7. These differences may occur because CO emission probes the dense interior of the cloud where the dynamics are much more influenced by gravity and embedded sources. D for cirrus clouds is consistent with a turbulent gas (Kolmogorov turbulence including the effects of intermittency — see Falgarone et al.). However, the strong dependence of D on the area range (Figure 5b) shows that for $l = 1$ and 0 (the smallest scales) D increases with increasing area reaching values about 2. This dependence suggests that the smallest features obey a Kolmogorov scaling law (D is close to the Bazell and Désert value) while the largest feature at $l = 0$ and 1 are filamentary-like structures. Visual inspection shows these features to consist

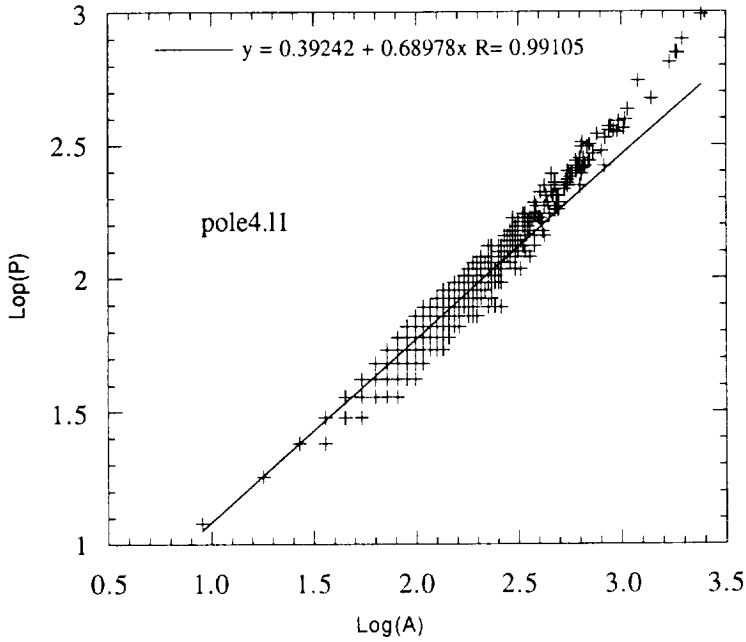

FIGURE 4 Determination of the Hausdorff dimension, D, and the shape factor, K, from plots of perimeter versus area for the $l = 1$ image. The fits are listed in the Figure.

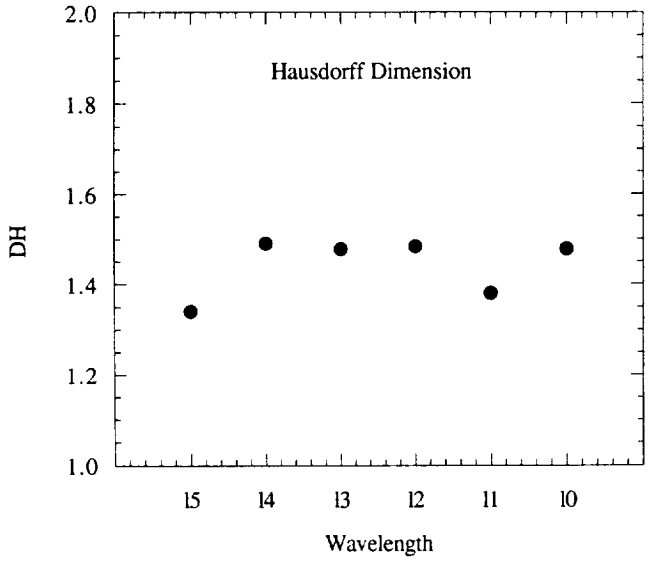

FIGURE 5a. Hausdorff dimension, D, versus l_n ($\approx$ wavelength, see Table 1) using all the features in each map.

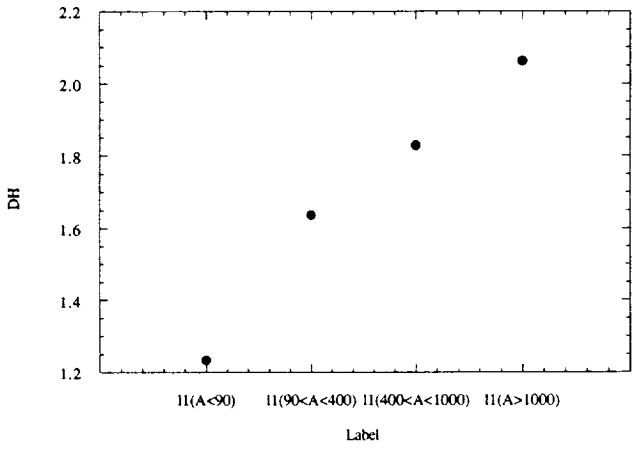

FIGURE 5b. Hausdorff dimension, D, versus different ranges in area for the $l = 1$ map.

of long single filaments and web-like structures. The latter are likely due to the overlap of separate features along the line of sight since the data have no velocity information and/or the merging of very many small scale features within the filters. Higher resolution 100 μm data is needed to test this hypothesis.

ACKNOWLEDGEMENTS

We thank Dr. T. N. Gautier for providing the IRAS images of the north polar cirrus used in this paper. RWW wishes to thank the Jet Propulsion Laboratory, California Institute of Technology, for hospitality and support as Distinguished Visiting Scientist. This work was carried out in part at the Jet Propulsion Laboratory, California Institute of Technology, under a contract with the National Aeronautics and Space Administration.

REFERENCES

Auriere, M. and Coupinot, G. 1989, *Proc. of the 1st ESO/ST-ECF Data Analysis Workshop*, eds. Grobs et al.

Bazell, D. and Désert, F. X. 1988, *ApJ*, **333**, 353

Coupinot, G., Hecquet, J., Auriere, M., and Fautaully, R. 1992, *A&A*, **259**, 701

Daubechies, I. 1992, *Ten Lectures on Wavelets*, CBMS-NSF Regional Conference Series in Applied Mathematics (Philadelphia: SIAM)

Dickman, R. L., Horvath, M. A., and Margulis, M. 1990, *ApJ*, **365**, 586

Falgarone, E., Phillips, T. G., and Walker, C. K., 1991, *ApJ*, **378**, 186

Farge, M. 1992, *Ann. Rev. Fluid Mech.*, **24**, 395

Gill, A. G. and Henriksen, R. N. 1990, *Ap. J. Letters*, **365**, L27

Grossman, A. and Morlet, J. 1987, *Mathematics and Physics, Lectures on Recent Results*, ed. L. Streit (World Scientific)

Houlahan, P. and Scalo, J. 1990, *Ap. J. Suppl.*, **72**, 133

Houlahan, P. and Scalo, J. 1992, *ApJ*, **393**, 172

Kleiner, S. C. and Dickman, R. L. 1984, *ApJ*, **286**, 255

Kleiner, S. C. and Dickman, R. L. 1985, *ApJ*, **295**, 466

Langer, W. D., Wilson, R. W., Goldsmith, P. F., and Beichman, C. A. 1989, *ApJ*, **337**, 355

Langer, W. D., Wilson, R. W., and Anderson, C. H. 1993, *ApJ*, **408**, L45

Martinez, V. J., Paredes, S., and Saar, E., 1993, *MNRAS*, **260**, 365

Press, W. H., Flannery, B. P., Teukolosky, S. A., and Vetterling, W. T. 1993, *Numerical Recipes 2nd Edition* (Cambridge University Press: Cambridge)

Simoncelli, E. P., Freeman, W. T., Adelson, E. H., and Heeger, D. J., 1992, *IEEE Trans., Info. Theory, Special Issue on Wavelets*, **38**, 587

Slezak, E., Bijaoui, A., and Mars, G. 1990, *A&A*, **227**, 301

Stutzki, J. and Gusten, R. 1990, *ApJ*, **356**, 513

Strang, G. T. 1989, *SIAM Review*, **31**, 614-627

Van der Wal, G. S. 1991, *The Sarnoff Pyramid Chip, Proc. Computer Architecture for Machine Perception*, (CAMP-91), Paris, p. 69

Wheelock, S. et al. 1994, *Explanatory Supplement to the IRAS Sky Survey Atlas*, (Pasadena:JPL), in press